Advances in Fiber-to-Chip Coupling and Cryogenic Packaging Technologies for Thin-Film Lithium Niobate Photonic Chips*[1]

Qi Liu(刘祺)[1,3],Yue Wang(王玥)[1*],Yuan-Da Wu(吴远大)[1,2,3],Jun-Ming An(安俊明)[1,2,3]

[1] *State Key Laboratory of Optoelectronic Materials and Devices, Institute of Semiconductors, Chinese Academy of Sciences, Beijing 100083, China*
[2] *Center of Materials Science and Optoelectronics Engineering, University of Chinese Academy of Sciences, Beijing 100049, China*
[3] *College of Materials Science and Opto-Electronic Technology, University of Chinese Academy of Sciences, Beijing 100049, China*
*wy1022@semi.ac.cn

Thin-film lithium niobate (TFLN) has emerged as a core material platform for next-generation integrated photonics, owing to its strong electro-optic effect ($\gamma_{33} \approx 30$ pm/V), second-order nonlinear optical coefficients, and broad transparency window spanning from the ultraviolet to the mid-infrared. However, the significant mode-field mismatch between sub-micrometer-scale lithium niobate waveguides and optical fibers renders efficient fiber-to-chip coupling a critical bottleneck for practical applications. This challenge is further exacerbated in cryogenic environments, where thermally induced stress causes misalignment at the coupling interface.

This paper systematically reviews the operating principles, performance metrics, and recent progress of the two mainstream coupling schemes on the TFLN platform—edge couplers and grating couplers. For edge coupling, structures including bi-layer inverse tapers, tri-layer inverse tapers, three-dimensional inverse tapers, trident structures, wedge-shaped couplers, double-layer metasurfaces, and multilayer silicon nitride-assisted couplers have achieved coupling losses below 0.5 dB/facet, with bandwidths covering the C+L bands and even extending into the visible range. For grating coupling, chirped gratings, apodized gratings, suspended gratings, hybrid silicon-platform gratings, and vertical gratings with bottom metal mirrors have attained sub-dB coupling losses. This paper also summarizes recent advances in cryogenic packaging technologies

[1] National Key R&D Program of China (Grant No. 2025YFA1212603)

and provides an outlook on future development directions.

Keywords:thin-film lithium niobate, edge coupler, grating coupler, cryogenic packaging

PACS： 42.82.Et, 42.79.Sz, 07.20.Mc

1 Introduction

Integrated photonics is experiencing rapid development in fields such as optical communications, microwave photonics, and quantum information processing[1]. Among the numerous material platforms for integrated photonics, thin-film lithium niobate (TFLN) has attracted considerable attention due to its unique material properties[2]. Lithium niobate possesses not only an ultra-wide transparency window covering the ultraviolet to mid-infrared (0.35–5 μm) but also a strong electro-optic effect ($\gamma_{33} \approx 30$ pm/V), second-order nonlinear optical coefficients, and piezoelectric properties, making it an ideal platform for high-speed electro-optic modulators, efficient wavelength converters, optical frequency combs, and quantum light sources[3]. In recent years, with the maturation of ion-slicing and dry-etching technologies, lithium niobate on insulator (LNOI) wafers have become commercially available. Waveguides fabricated on this platform exhibit strong optical confinement at the sub-micrometer scale[9], greatly promoting the development of highly integrated, high-performance photonic chips[11].

A major unresolved challenge, however, is the efficient optical interconnection between TFLN waveguides and standard single-mode fibers (SSMF)[13]. A typical TFLN ridge waveguide has a mode-field area of less than 1 μm², whereas the mode-field diameter (MFD) of an SSMF at 1550 nm is approximately 10 μm. The resulting mode-field mismatch leads to a coupling loss as high as 10 dB per facet for direct coupling[14]. Such severe insertion loss significantly degrades system performance and, particularly for quantum applications that are extremely sensitive to photon loss, represents a primary obstacle to large-scale integration[15].

The mainstream strategies for addressing this mode-field mismatch fall into two categories: edge coupling and grating coupling[16]. Edge couplers use adiabatic

tapered waveguides at the chip edge to gradually expand the sub-micrometer waveguide mode to match the fiber mode, thereby enabling efficient, broadband, and polarization-insensitive optical transmission. Grating couplers, in contrast, employ periodic diffraction structures on the chip surface to couple light between the fiber and the on-chip waveguide at a specific angle, offering advantages such as flexible placement, requiring no facet polishing, and wafer-level testability[18]. The two schemes involve different trade-offs in terms of coupling efficiency, operating bandwidth, polarization dependence, alignment tolerance, and fabrication complexity, and are thus suitable for different application scenarios[19].

In many emerging fields such as quantum computing, superconducting single-photon detection, and quantum sensing, devices often need to operate at cryogenic temperatures down to a few kelvin (K) or even millikelvin (mK) to suppress thermal noise, extend quantum coherence times, or exploit superconducting phenomena[20]. When a photonic chip is cooled from room temperature to cryogenic temperature, the differences in the coefficients of thermal expansion among the fiber, chip substrate, and cured adhesive induce significant thermal stress. This can cause misalignment at the coupling interface that was precisely aligned at room temperature, and in extreme cases, complete device failure. Moreover, cryostats are typically enclosed and space-limited, making in-situ realignment at cryogenic temperatures impractical[23]. Therefore, developing a cryogenic-compatible packaging technology that can perform alignment and fixation at room temperature while maintaining stable coupling performance over a wide temperature range is essential for advancing the application of lithium niobate photonic chips in quantum technologies[24].

This paper aims to provide a systematic review of recent advances in fiber-to-chip coupling and cryogenic packaging technologies for lithium niobate photonic chips. It covers the structural design, fabrication processes, and key performance breakthroughs of edge couplers and grating couplers, with a particular focus on cryogenic-compatible packaging technologies and their typical applications. The paper concludes by summarizing current challenges and offering perspectives on future development directions.

2 Key Metrics for Coupling Performance Evaluation

The performance of fiber-to-chip coupling is typically assessed using the following key metrics.

(1) Coupling Efficiency. Defined as the ratio of the optical power emerging from the fiber that is successfully delivered to the on-chip waveguide through the coupler, this is the most direct and important performance parameter. Since on-chip optical power is difficult to measure directly, experiments often employ a loopback configuration (fiber → coupler → waveguide → coupler → fiber). Assuming equal input and output coupling efficiencies, the single-facet coupling efficiency can be estimated from[26]

$$\eta = \sqrt{\frac{P_{out}}{P_{in}}} \tag{1}$$

where P_{out} and P_{in} are the output and input powers, respectively. The main physical factors affecting coupling efficiency are the mode overlap integral and the directionality. The former characterizes the match between the fiber mode and the coupler radiation mode; the latter refers to the fraction of diffracted optical power directed along the desired path (upward into the fiber or downward into the waveguide).

(2) Coupling Bandwidth. This metric characterizes the spectral range over which the coupler can operate effectively. Owing to the wavelength dependence of material dispersion and waveguide structural parameters, coupling efficiency typically exhibits a spectral dependence. The 1-dB and 3-dB bandwidths are usually defined as the wavelength ranges over which the coupling efficiency drops by 1 dB and 3 dB from its peak value, respectively[27]. Broadband couplers are essential for multi-wavelength applications such as wavelength-division multiplexing and nonlinear optics.

(3) Misalignment Tolerance. This is defined as the tolerance to displacement from the optimal alignment position before the coupling efficiency degrades by a specified amount, typically expressed as the spatial offset that causes an additional loss of 1 dB or 3 dB[28]. This metric is particularly important for packaging stability: when a device undergoes temperature cycling, thermal expansion mismatch between

materials introduces positional shifts at the coupling interface, and a high misalignment tolerance can significantly mitigate the resulting performance degradation. For horizontally coupled edge couplers, tolerances in both the transverse (X/Y) and longitudinal (Z) directions must be considered; for vertically coupled grating couplers, the main concerns are fiber tilt angle and horizontal position offset. Quantitatively, when the fiber and coupler modes are approximated as two identical Gaussian fields with mode-field radius w_0 and a relative lateral offset δ, their power coupling follows $\eta(\delta) = \exp(-\delta^2/w_0^2)$, which corresponds to an excess loss $L_{ex}(\delta) = -10\cdot\lg\ \eta \approx 4.34(\delta/w_0)^2$ dB. This Gaussian-overlap relation directly connects a thermally induced displacement (Section 4) to the resulting loss penalty: the excess loss grows quadratically with the offset once δ becomes comparable to w_0, which is why a large misalignment tolerance is indispensable for packaging stability.

(4) Scalability. This metric measures the ability of a coupling scheme to support multi-channel, high-density parallel optical interconnects. As photonic chips become increasingly complex, dozens or even hundreds of optical ports may need to be integrated on a single chip. Compatibility with commercial fiber arrays (FAs) and the ability to achieve low-crosstalk multi-channel coupling are important indicators of a coupling scheme's potential for large-scale deployment.

(5) Polarization Dependence. This reflects the difference in coupling response to TE and TM polarization states. In fiber-optic communications, the signal polarization state is generally random, so couplers with low polarization-dependent loss (PDL) are required. For some quantum optics applications that require maintaining a specific polarization state, couplers with high polarization selectivity may be deliberately chosen. Lithium niobate is an anisotropic crystal, and the effective refractive indices for TE and TM modes differ, which adds to the design challenge of achieving low PDL coupling[29].

(6) Fabrication Compatibility. This examines whether the coupler fabrication is compatible with standard waveguide device process flows. For edge couplers, this involves issues such as the alignment accuracy of multi-layer lithography and facet polishing quality; for grating couplers, it involves etch depth control and minimum

feature size limitations[30]. An ideal coupling scheme should maximize performance while minimizing reliance on specialized processing steps.

3 Research Progress on Fiber-to-Chip Coupling Technologies for Lithium Niobate Photonic Chips

3.1 Edge Couplers

The core design concept of edge couplers is to use an adiabatic tapered waveguide structure to achieve a smooth transition from the sub-micrometer waveguide mode to the fiber mode. The basic principle can be understood through the mode overlap integral; the coupling efficiency is given by

$$\eta = \frac{|\iint E_{fiber} \cdot E_{waveguide} dS|^2}{\iint |E_{fiber}|^2 dS \cdot \iint |E_{waveguide}|^2 dS} \tag{2}$$

where E represents the electric field distribution and the integration is performed over the overlapping area of the coupling cross-section[31]. To achieve adiabatic mode conversion, the cross-sectional dimensions of the tapered structure must vary gradually enough to avoid mode discontinuity or energy reflection—which typically requires taper lengths on the order of hundreds of micrometers.

Achieving high-efficiency edge coupling on the TFLN platform presents a particular fabrication challenge: dry etching of lithium niobate typically produces a non-vertical sidewall angle of about 60°, giving the taper tip a trapezoidal rather than a rectangular cross-section. This morphological feature significantly affects the mode-field shape and size at the tip, not only increasing the difficulty of matching the fiber mode but also making the mode conversion efficiency of multi-layer structures extremely sensitive to overlay accuracy. To mitigate this limitation, numerous innovative structures have been proposed, such as bi-layer/tri-layer inverse-taper edge couplers, 3D inverse-taper edge couplers, trident edge couplers and double-layer metasurface edge couplers. The sensitivity to inter-layer overlay can be quantified with the same overlap argument: the mode-conversion penalty stays below 0.1 dB as long as the relative lateral shift is much smaller than the mode-field radius at the expanded taper tip. This is confirmed experimentally—the DUV-compatible bi-layer

taper of Zheng et al. [31] tolerates an overlay as large as ±300 nm with negligible added loss, and the 3D crossed taper [36] sustains a ±300 nm overlay with an extra loss below 0.06 dB, which is 6–15 times the ±20–50 nm overlay accuracy of typical electron-beam lithography and thus decouples performance from lithographic alignment precision. Likewise, the multilayer SiN-assisted coupler retains above 85% coupling efficiency under TFLN waveguide width fluctuations of ±200 nm and thickness fluctuations of ±30 nm. These data show that geometric innovations (crossed three-dimensional tips, compliant auxiliary layers) relax overlay requirements far more effectively than merely reducing the tip linewidth.

3.1.1 Bi-layer Inverse-taper Edge Coupler

The bi-layer inverse taper is the foundational architecture for TFLN edge couplers. It was first proposed and experimentally demonstrated by He et al. [32]and Hu et al. [33]. As shown in Fig. 1(a), the typical structure consists of a fully etched bottom lithium niobate inverse taper (typically 200–300 nm thick), which gradually "draws" the input optical field from the cladding waveguide into the lithium niobate layer, and a shallow-etched top lithium niobate inverse taper (ridge height typically 200–250 nm), which completes the transition to the standard ridge waveguide mode. Some designs also introduce an intermediate cladding waveguide with a refractive index between that of lithium niobate and silicon dioxide, such as silicon oxynitride (SiON) or the polymer SU8, to further optimize mode matching[33].

Hu et al. [33]achieved efficient coupling to ultra-high numerical aperture fiber (UHNAF, MFD ≈ 3.2 μm) by cladding the TFLN taper structure with a SiON rectangular waveguide with a refractive index of approximately 1.56. As shown in Figs. 1(b) and 1(c), the structure comprises three functional sections: a lithium niobate slab narrowing section, a top inverse taper (ridge width tapering from 0.26 μm to 0.15 μm), and a bottom inverse taper (width gradually tapering to a 0.15 μm tip). The measured TE and TM edge coupling losses were as low as 0.54 and 0.59 dB/facet, respectively, and both remained below 1 dB/facet over the wavelength range of 1527–1630 nm. Notably, the device also exhibited excellent thermal stability, with coupling

efficiency degradation of less than 0.01 dB over a temperature cycling test from -45 to 75 °C.

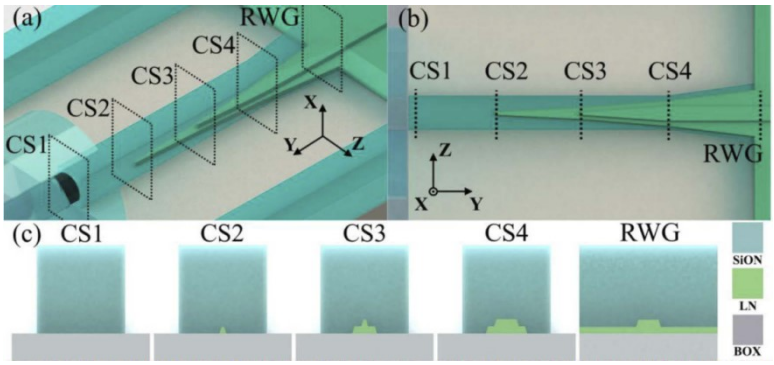


Fig. 1 Schematic of the SiON-clad edge coupler. (a) Schematic of the bi-layer inverse-taper edge coupler; (b) Top view of the edge coupler; (c) Cross-sectional view of the coupler.

Around the same time, Ying et al. [34]used SU8 polymer as the cladding waveguide to achieve a coupling loss as low as 0.5 dB/facet between a lithium niobate modulator and a lensed fiber. The bottom inverse taper tip width was set to 120 nm and the top inverse taper tip width to 150 nm. An important contribution of this work is the first experimental demonstration of monolithic integration of a high-efficiency edge coupler with a high-performance Mach-Zehnder modulator (MZM). The fabricated modulator exhibited a total on-chip loss of approximately 3 dB, a half-wave voltage of 2.36 V, an electro-optic bandwidth of 60 GHz, and successfully demonstrated 200 Gbit/s discrete multi-tone modulation signal transmission.

In a more recent study, Zheng et al. [31] designed and demonstrated a bi-layer inverse-taper edge coupler compatible with deep ultraviolet lithography for cost-sensitive applications such as fiber-optic gyroscopes. As shown in Fig. 2, unlike previous works that used UHNAF or lensed fibers, this design is specifically adapted to standard single-mode fibers with an MFD of 6 μm, thus avoiding the use of expensive specialty fibers. The bottom inverse taper tip width was increased to about 200 nm (matching the linewidth limit of deep ultraviolet lithography), the top inverse taper tip width was about 200 nm, and the taper length was 300 μm. The measured coupling loss at 1310 nm was 2.3 dB/facet (corresponding to a coupling efficiency of about 59%), and the lateral overlay misalignment tolerance between the top and

bottom tapers was as high as ±300 nm with negligible additional loss. This work minimizes the lithographic precision requirements while maintaining adequate performance, offering a viable path toward low-cost, high-volume manufacturing of lithium niobate photonic chips.

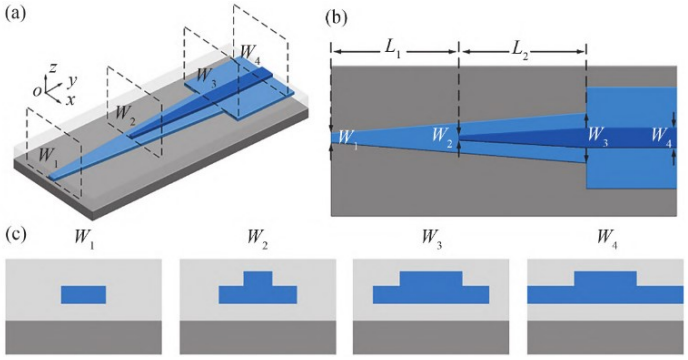


Fig. 2 Bi-layer inverse-taper edge coupler adapted to standard single-mode fiber (MFD = 6 μm). (a) 3D schematic; (b) Top view; (c) Cross-sectional view.

3.1.2 Tri-layer Inverse-taper Edge Coupler

While bi-layer inverse tapers achieve high coupling efficiency, there remains room for improvement in operating bandwidth and polarization performance. This is particularly true for nonlinear optical applications such as second-harmonic generation, where the edge coupler must simultaneously handle two widely separated wavelengths: the near-infrared pump (e.g., 1550 nm) and the near-visible second harmonic (e.g., 775 nm). Conventional bi-layer tapers typically require a bottom tip width of less than 100 nm to achieve sub-3 dB coupling loss in the visible band, a dimension approaching the limit of electron-beam lithography and making fabrication yield difficult to guarantee.

To address this challenge, Liu et al. [35] proposed a tri-layer TFLN inverse-taper structure (Tri-Layer SSC). As shown in Fig. 3, this structure builds on the conventional bi-layer taper by splitting the original bottom layer into two thin tapered layers in series (each about 90 nm thick, 180 nm total). This design keeps the overall tip width of the three layers at 100 nm while reducing the effective tip thickness of each individual layer, thereby enabling adiabatic conversion of shorter-wavelength modes. Combined with a suspended SiO_2 cladding waveguide, this coupler achieved

coupling losses of 1 dB/facet at 1550 nm and 3 dB/facet at 775 nm, with a bandwidth exceeding 100 nm. A 5-mm-long periodically poled lithium niobate waveguide integrated with this coupler achieved a fiber-to-fiber second-harmonic generation normalized conversion efficiency as high as 1027% $W^{-1}\cdot cm^{-2}$ (corresponding to an on-chip efficiency of 3256% $W^{-1}\cdot cm^{-2}$), an improvement of 2–3 orders of magnitude over the previous best results. This work clearly demonstrates the key enabling role of high-efficiency broadband coupling for nonlinear functional devices.

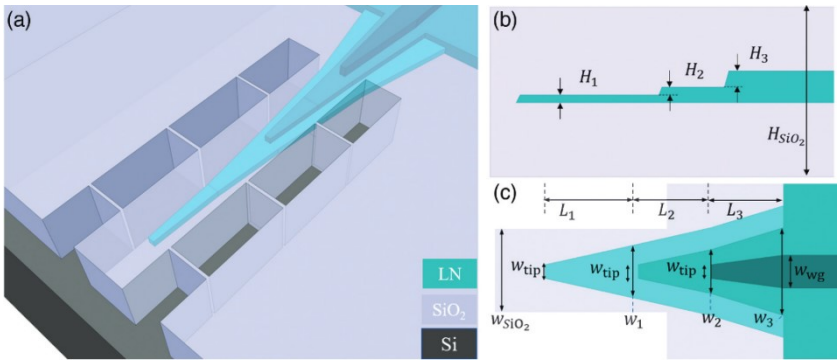


Fig. 3 Schematic of the tri-layer inverse taper edge coupler. (a) 3D schematic structure of the coupler; (b) Cross-sectional view of the coupler; (c) Top view of the coupler.

3.1.3 Three-Dimensional Inverse-taper Edge Coupler

Although planar inverse taper structures have made significant progress, conventional bi-layer tapers remain subject to inherent geometric limitations that restrict further loss reduction, bandwidth broadening, and fabrication robustness. Specifically, at the interface between the two taper layers, the non-vertical sidewalls cause an inherent mode mismatch between the top ridge waveguide tip and the bottom inverse taper, leading to unavoidable mode conversion loss and stringent overlay accuracy requirements.

To overcome this bottleneck, Chen et al. [36] proposed an innovative three-dimensional (3D) bi-layer taper structure based on a crossed layout. As shown in Fig. 4, the key feature of this design is that the tips of the top and bottom inverse tapers are not completely collinear; instead, a 3D gradually varying tip is formed through an obliquely crossed transition section. The superposition of the two mask patterns in the crossing region ultimately produces a geometrically infinitely sharp 3D tip at the coupling interface, completely eliminating the tip "blunting" effect that

plagues conventional bi-layer tapers due to minimum feature size limitations. This 3D tapering ensures fully adiabatic mode conversion for both TE and TM polarizations.

Experimental results show that when coupled to a high-NA fiber with an MFD of 4.8 μm, this 3D tapered edge coupler achieved best TE and TM edge losses of 0.29 dB and 0.24 dB, respectively, with a 0.5-dB coupling bandwidth exceeding 180 nm and a polarization-dependent loss below 0.17 dB over this range. More importantly, the structure exhibited excellent overlay tolerance—the lateral misalignment tolerance between the top and bottom lithium niobate patterns was as high as ±300 nm (corresponding to an additional loss below 0.06 dB), far exceeding the overlay accuracy range of typical electron-beam lithography equipment (±20 to ±50 nm). This makes the design promising for scalable manufacturing. Through clever geometric design, this work completely eliminates the stringent tip linewidth requirement for edge couplers, marking a major breakthrough in the overall performance of TFLN edge coupling technology.

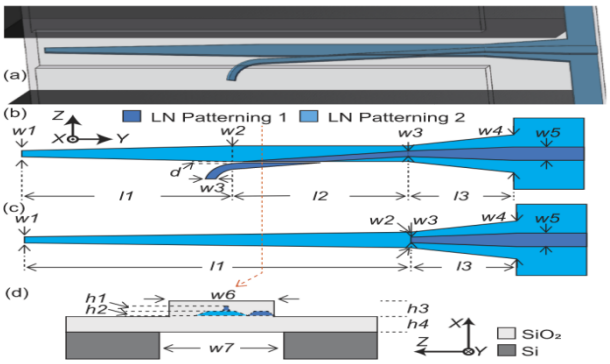


Fig. 4 Schematic of the three-dimensional inverse-taper edge coupler. (a) 3D schematic structure; (b) Top view of the crossed bi-layer taper; (c) Top view of the conventional centered bi-layer taper; (d) Cross-sectional view of the crossed bi-layer taper.

3.1.4 Trident Edge Coupler

To meet the demand for high-tolerance interconnection between standard single-mode fibers and TFLN chips, a TFLN edge coupler based on a silicon nitride trident structure has been proposed [37]. As shown in Fig. 5, the core idea is to use the silicon nitride trident structure as an intermediate layer: the optical mode of the TFLN waveguide is first adiabatically coupled into the silicon nitride waveguide, and the large mode field of the silicon nitride waveguide is then used for efficient matching

with the standard fiber. Simulation results show that in the C+L band, the TE mode coupling loss is below 0.71 dB, the TM mode coupling loss is below 0.91 dB, the polarization-dependent loss is below 0.41 dB, and the mode-field diameter is greater than 8 μm.

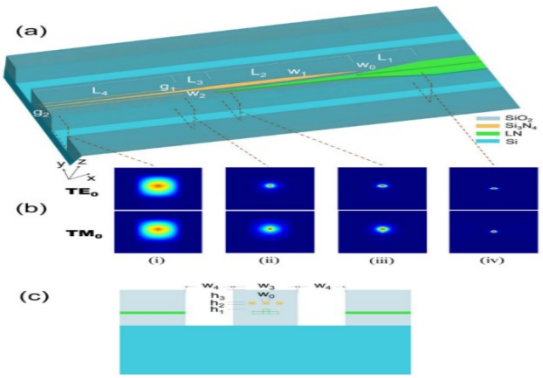


Fig. 5 Schematic of the trident edge coupler. (a) Schematic of the trident edge coupler; (b) TE_0/TM_0 mode-field distributions at four cross-sections: (i) left end face of the trident structure, (ii) right end face of the trident structure, (iii) coupling region between Si_3N_4 and the LN waveguide, (iv) LN waveguide; (c) Cross-sectional schematic of the trident structure.

3.1.5 Wedge-Shaped Edge Coupler

Ma et al. [38] reported a low-loss broadband wedge-shaped thin-film lithium niobate edge coupler compatible with standard i-line lithography in Optics Letters. The TFLN waveguide serves as the intermediate layer to achieve interconnection with standard single-mode fiber. The coupler achieved a coupling loss of 0.78 dB at 1550 nm and a 1-dB bandwidth of 150 nm. Fabricated by low-cost i-line lithography compatible with CMOS manufacturing processes, this coupler clearly demonstrates the feasibility of achieving low-loss edge coupling through standard lithography.

3.1.6 Double-Layer Metasurface Edge Coupler

Wang et al. [39] proposed an all-dielectric double-layer metasurface edge coupler in Scientific Reports. As shown in Fig. 6, this structure precisely manipulates the optical wavefront using subwavelength structural units, directly reshaping the Gaussian beam from the fiber into an elliptical profile that closely matches the TFLN ridge waveguide mode. Finite-difference time-domain simulations confirm that this coupler achieves a coupling loss below 1.9 dB/facet over the full communication band (1460–1630 nm), with a minimum loss of only 0.6 dB/facet at 1550 nm, and vertical

and horizontal alignment tolerances of ±1 μm and ±2.5 μm, respectively.

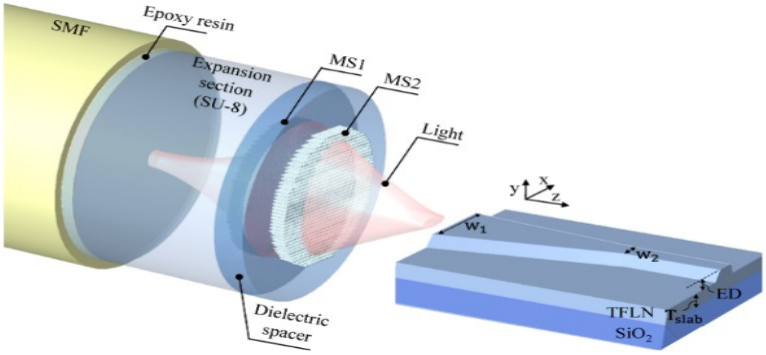


Fig. 6 Schematic of the double-layer metasurface edge coupler.

3.1.7 Multilayer Silicon Nitride-Assisted Edge Coupler

Tang et al. [40] reported a lithographically fabricated multilayer silicon nitride-assisted edge coupler in Optics Letters. This device integrates multilayer silicon nitride waveguides as an auxiliary transition layer onto the TFLN platform. The basic principle is to use the higher refractive index of silicon nitride and its lower sensitivity to fabrication errors to construct a multilayer adiabatic transition structure that gradually expands the small mode field of the TFLN waveguide to match the fiber. The coupling efficiency can be maintained above 85% even with TFLN waveguide width deviations of ±200 nm and height deviations of ±30 nm. The device achieved a coupling loss of 1.2 dB/facet and a wavelength-dependent loss of less than 0.4 dB/facet over the entire C-band, with a 3-dB alignment tolerance of ±3 μm.

Table 1 summarizes the cladding materials, coupling losses, bandwidths, and other key parameters of TFLN edge couplers reported in recent years.

Table 1. Summary of typical TFLN edge couplers

Structure type	Cladding/ aux.	Fiber type	Coupling loss (dB/facet)	Bandwidth (nm)	PDL (dB)	Alignment / overlay tolerance	Data type	Fabrication complexity	Ref.
Bi-layer inverse-taper	SiON	UHNAF (MFD 3.2 μm)	TE 0.54 TM 0.59 (1530-1565nm)	103 (1-dB)	0.05	—	E	Moderate (bi-layer EBL)	[33]
Bi-layer inverse-taper	SU8	Lensed fiber	0.5 (1550nm)	—	—	—	E	Moderate (bi-layer,	[34]

(modulator-integrated) Structure type	Cladding/aux.	Fiber type	Coupling loss (dB/facet)	Bandwidth (nm)	PDL (dB)	Alignment / overlay tolerance	Data type	monolithic MZM) Fabrication complexity	Ref.
Tri-layer inverse-taper	Suspended SiO_2	—	1（1550nm） 3（775nm）	—	—	±300 nm overlay, negligible loss	E	Low (deep-UV lithography)	[35]
3D crossed bi-layer taper	SiO_2	High-NA (MFD 4.8 μm)	TE 0.29 TM 0.24 （1530-1625nm）	180 (0.5-dB)	—	100-nm triple tip	E	High (tri-layer, suspended)	[36]
Trident structure	Si_3N_4	SSMF	TE <0.71 TM <0.91 （1530-1625nm）	—	<0.17	±300 nm overlay, <0.06 dB	E	Low–moderate (EBL, relaxed overlay)	[37]
Wedge-shaped	SiO_2	SMF	0.78 （1550nm）	150 (1-dB)	<0.41	—	S	Moderate (SiN interlayer)	[38]
Double-layer metasurface (DLMS)	—	SMF	0.6 (simulated)	170 （1.9-dB）	—	—	E	Low (i-line lithography)	[39]
Multilayer SiN-assisted	SiN	SMF	1.2	35 （0.4-dB）	—	±1 μm vertical; ±2.5 μm horizontal	S	High (metasurface)	[40]

Note: S, simulated; E, experimental.

Table 1 summarizes the main structural families of TFLN edge couplers and compares their key performance metrics.

(i) Coupling loss: the lowest measured losses are delivered by adiabatic bi/tri-layer tapers with an expanded intermediate mode—the 3D crossed taper reaches 0.29/0.24 dB per facet for TE/TM , followed by the SU8-clad bi-layer taper (0.5 dB[34]) and the SiON-clad design (0.54/0.59 dB[33]); simulation-only designs (trident[37], metasurface) predict comparable values that still await experimental verification.

(ii) Bandwidth and spectral coverage: conventional bi-layer tapers cover the C+L band (≈103 nm at 1-dB[33]), the 3D crossed taper extends the 0.5-dB bandwidth to 180 nm[36], and the tri-layer architecture uniquely supports dual-band near-infrared/visible operation (1 dB at 1550 nm and 3 dB at 775 nm[35]), which is essential for nonlinear frequency-conversion devices.

(iii) Fiber compatibility: early high-performance designs rely on high-NA or lensed specialty fibers (MFD 3.2–4.8 μm), whereas the recent trident, wedge, metasurface and multilayer-SiN designs deliberately match standard single-mode fibers (MFD 6–10 μm), trading a modest loss increase for markedly lower packaging cost.

(iv) Polarization: explicit TE–TM balancing remains difficult; the reported PDL ranges from 0.05 dB for the mode-matched SiON bi-layer and below 0.17 dB for the 3D crossed tape to below 0.41 dB for the simulated trident , indicating that symmetric three-dimensional mode expansion is the most effective route to polarization insensitivity.

(v) Alignment tolerance versus manufacturability: a clear trade-off emerges—the lowest-loss devices still require electron-beam lithography and multi-layer alignment, whereas i-line and deep-UV compatible structures, together with the overlay-robust 3D and SiN designs, sacrifice roughly 0.5–1.5 dB to gain wafer-scale manufacturability and relaxed tolerances (±300 nm inter-layer overlay; ±3 μm fiber alignment).

Taken together, these comparisons indicate that TFLN edge-coupler design is governed by a multi-objective trade-off among coupling loss, bandwidth, polarization dependence, fiber compatibility, alignment tolerance, and fabrication complexity; the optimal architecture is therefore application-specific, with multi-layer adiabatic tapers favored for sub-dB loss and broadband operation, lithography-compatible relaxed-tip designs for wafer-scale manufacturing, and tri-layer architectures for visible/near-infrared dual-band applications.

3.2 Grating Couplers

Unlike edge couplers, grating couplers achieve vertical optical interconnection between the fiber and the waveguide through periodically etched diffraction gratings on the chip surface. The operating principle is based on the Bragg phase-matching condition:

$$k_0 \sin\theta = \frac{\beta + 2\pi q}{\lambda} \tag{3}$$

where k_0 is the free-space wave vector, θ is the incidence angle (relative to the chip surface normal), β is the propagation constant of the waveguide mode, q is the diffraction order, and Λ is the grating period [41]. When this condition is satisfied, incident light diffracted by the grating can achieve phase-matched energy coupling to the waveguide mode.

On the TFLN platform, the main challenge for grating couplers arises from the relatively low refractive index of lithium niobate (about 2.21 at 1550 nm, lower than silicon's 3.45) and the typically ~60° non-vertical etch sidewalls. These factors together result in weaker grating diffraction intensity compared with the SOI platform, limiting both coupling efficiency and bandwidth [42]. To overcome these inherent limitations, researchers have continuously pushed the performance boundaries of TFLN grating couplers through non-uniform grating designs, heterogeneous material integration, and inverse optimization. Representative structures include chirped grating couplers, hybrid silicon–TFLN platform vertical grating couplers, suspended grating couplers, apodized grating couplers, and vertical grating couplers with bottom metal mirrors.

3.2.1 Chirped Grating Coupler

Compared with conventional uniform gratings, non-uniform gratings can better match the diffracted optical mode field to the Gaussian mode field of the fiber by dynamically adjusting the grating period and fill factor, thereby significantly improving coupling efficiency. Kang et al. [43] adopted a structure combining chirped gratings with uniform gratings. Through simulation optimization to determine the duty cycle and corresponding period of each grating groove, the TE-mode simulation coupling loss near 1550 nm was 0.52 dB, and the lowest measured coupling loss was 1.43 dB (at 1552.6 nm), with the TM mode at 2.10 dB (at 1547.2 nm).

3.2.2 Hybrid Silicon–TFLN Platform Vertical Grating Coupler

To circumvent the difficulty of direct TFLN etching, Wang et al. [44] designed a high-performance vertical grating coupler on a hybrid silicon–TFLN platform using inverse design. As shown in Fig. 7, the structure employs cascaded double-layer

chirped silicon gratings combined with an adiabatic Si–TFLN transition structure, achieving a sub-dB coupling loss of 0.86 dB and a 3-dB bandwidth of 45 nm under vertical incidence (0°) and quasi-TE mode, without the need for a metal mirror.

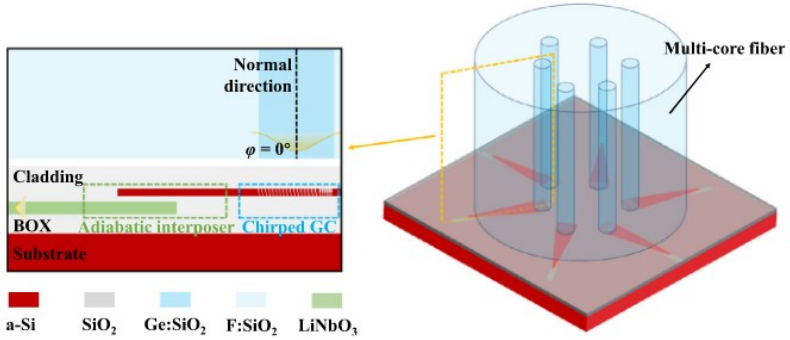


Fig. 7 Conceptual diagram of a hybrid a-Si–TFLN device packaged with a multi-core fiber and the corresponding cross-sectional view of the proposed cascaded grating coupler. φ is defined as the emission angle relative to the grating normal direction. For a vertical grating coupler, φ = 0°.

Suraj et al. [45] designed another high-efficiency hybrid grating coupler based on a silicon overlay, as shown in Fig. 8. By using the silicon overlay to enhance diffraction contrast, simulated peak coupling efficiencies of 84% (0.76 dB) at 775 nm and 81% (0.9 dB) at 1552 nm were achieved. Experimental verification showed a measured coupling efficiency of 61.66% at the 780 nm Rb absorption line and 75.16% at 1520 nm—the highest value reported to date for TE grating couplers on the TFLN platform without metal assistance.

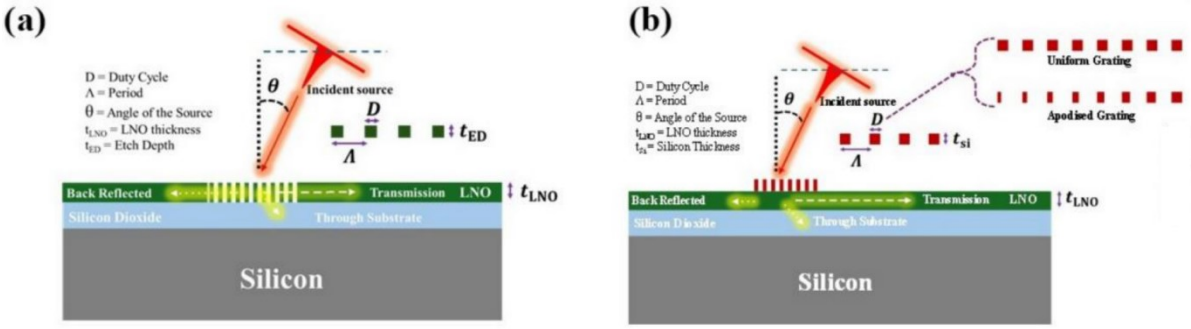


Fig. 8 Schematic of the high-efficiency hybrid grating coupler based on a silicon overlay. (a), (b) Schematic of the TFLN grating coupler with uniform and apodized configurations of the hybrid silicon grating coupler.

3.2.3 Suspended Grating Coupler

To address the light coupling challenge for fully etched photonic devices on ultra-thin LNOI (thickness 300 nm or less), suspended grating couplers remove the

substrate material beneath the grating to suspend the grating structure, thereby improving mode matching and directionality [46]. Lu et al. [47] proposed and demonstrated a high-performance suspended grating coupler on 300-nm-thick ultra-thin X-cut LNOI, as shown in Fig. 9. The optimized design achieved a coupling loss of 3.5 dB at 1546.24 nm, with a 1-dB bandwidth of 70 nm and a 3-dB bandwidth exceeding 90 nm, while exhibiting good fabrication tolerance. This work effectively solves the light coupling challenge on the ultra-thin LNOI platform, providing a practical and scalable solution for coupling to photonic crystal waveguides and other suspended photonic devices.

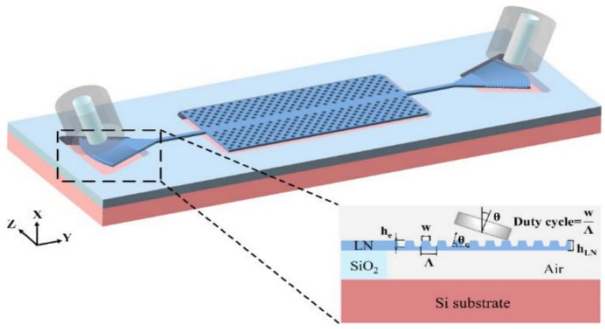


Fig. 9 3D schematic of a suspended grating coupler on ultra-thin LN for 2D photonic crystal waveguides. The inset shows the 2D cross-sectional view used for simulation, with all structural parameters labeled.

3.2.4 Apodized Grating Coupler

Apodized grating couplers linearly optimize the grating period and fill factor to make the radiated mode-field distribution of the grating closer to the Gaussian mode field of the fiber, thereby effectively improving the mode-matching efficiency between the fiber and the waveguide [48].

Fang et al. [49] demonstrated a high-efficiency apodized grating coupler on a 600-nm-thick X-cut TFLN platform, with careful consideration of fabrication capability. Without using any mirrors or hybrid materials, this device achieved a coupling efficiency of 50.47% at 1555 nm through a single lithography and etching step, setting a new efficiency benchmark for grating couplers on the 600-nm-thick TFLN platform. This result clearly demonstrates that high-efficiency fiber-to-chip vertical coupling can be achieved on the standard TFLN platform through proper

apodized grating design, without relying on complex metal reflector layers or heterogeneous material integration.

3.2.5 Vertical Grating Coupler with Bottom Metal Mirror

Introducing a metal reflector layer at the bottom of the grating coupler is an effective way to improve coupling efficiency. The principle is to reflect the optical power radiated downward to the substrate back to the grating region for secondary coupling. Wang et al. [50] designed and fabricated a vertical coupling grating coupler with a metal mirror on the X-cut TFLN platform, as shown in Fig. 10. The grating coupler uses a Cr/Au/Cr metal reflector layer structure. Through optimization of the grating period, duty cycle, and metal layer thickness, perfect vertical coupling to standard single-mode fiber was achieved. Experimental results show that the device exhibits excellent coupling performance in the 1550 nm communication band, facilitating wafer-level testing and packaging of TFLN photonic chips. While maintaining high coupling efficiency, this scheme avoids complex fiber angle alignment requirements and has good fabrication compatibility and scalability. A TFLN Mach-Zehnder modulator based on this coupler achieved a fiber-to-fiber total loss of 6.5 dB, a 3-dB electro-optic bandwidth exceeding 67 GHz, and 100 Gbit/s OOK data transmission.

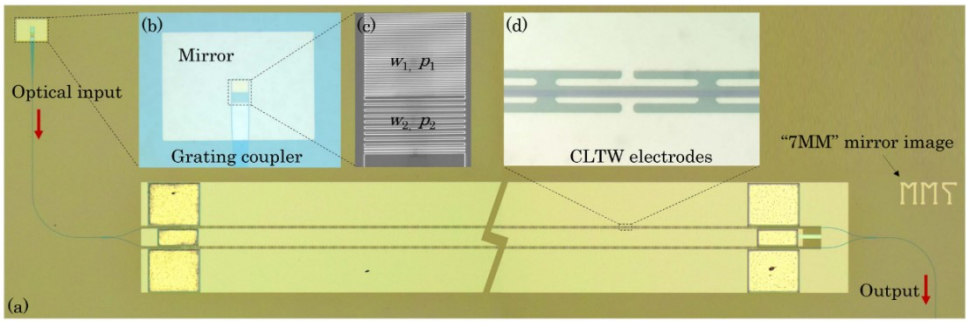


Fig. 10 Optical and scanning electron microscope images of the fabricated device. (a) Entire device; (b)–(c) Grating couplers; (d) Magnified view of the modulation region. The output grating coupler is not shown.

Table 2 summarizes the coupling losses, bandwidths, and other key parameters of TFLN grating couplers reported in recent years.

Table 2. Summary of typical TFLN grating couplers

Structure type	Platform /material	Coupling loss (dB)	Bandwidth (nm)	Data type	Alignment tolerance	Fabrication complexity	Ref.
Chirped grating (PSO+BPNN optimized)	TFLN	0.52 (sim.); 1.43 TE @1552.6 nm; 2.10 TM @1547.2 nm (exp.)	—	S/E	—	Moderate (non-uniform EBL grating)	[43]
Structure type	**Platform /material**	**Coupling loss (dB)**	**Bandwidth (nm)**	**Data type**	**Alignment tolerance**	**Fabrication complexity**	**Ref.**
Hybrid Si-TFLN vertical grating	Si-TFLN	0.86 @1550 nm (quasi-TE, vertical 0°)	45 (3-dB)	E	vertical incidence	Moderate (double Si layer + transition)	[44]
Hybrid Si overlay grating	Si overlay + TFLN	0.76@775 nm / 0.9@1552 nm (sim.); 1.24@1520 nm (75.16%, exp.)	40 (3-dB)	S/E	—	Moderate (Si overlay deposition)	[45]
Suspended grating	300 nm ultra-thin X-cut LNOI	3.5 @1546.24 nm	70 (1-dB); >90 (3-dB)	E	robust to fab. errors	Moderate (suspension release)	[47]
Apodized grating	600 nm X-cut TFLN	2.97 (50.47%) @1555 nm	—	E	—	Low (single etch, no mirror)	[49]
Vertical grating with bottom metal mirror	X-cut TFLN + Cr/Au/Cr	6.5 (fiber-to-fiber of full MZM link) @1550 nm	—	E	perfectly vertical	Moderate (metal reflector process)	[50]

Note: S, simulated; E, experimental. The 6.5 dB value for the bottom-metal-mirror grating refers to the fiber-to-fiber loss of the complete modulator link, not a single grating coupler.

Table 2 compares the main approaches to TFLN grating couplers, which fall into three categories. Intrinsic TFLN gratings based on non-uniform geometries (chirped, apodized and suspended) require neither foreign materials nor mirrors. The apodized design achieves 50.47% (2.97 dB) with a single lithography/etch step on standard

600-nm TFLN, representing the most fabrication-friendly option, while the suspended design addresses coupling on 300-nm ultra-thin LNOI at the cost of 3.5 dB and an additional release process. Heterogeneous-integration approaches, such as cascaded silicon chirped gratings and silicon overlays, exploit the high index contrast of silicon to enhance diffraction, achieving a measured 0.86 dB[44] and 75.16% at 1520 nm[45], respectively, at the expense of additional deposition and mode-transition sections. The bottom-metal-mirror approach[50] reflects downward radiation and enables perfectly vertical, wafer-level-testable coupling, but adds metal processing and results in a 6.5 dB fiber-to-fiber link loss. Across these approaches, the discrepancy between simulated and measured results is typically 0.3–0.9 dB, mainly due to etch-depth errors, non-vertical sidewall angles, and dimensional deviations. This gap should be considered when comparing predicted and demonstrated performance. Grating bandwidths are limited to approximately 40–90 nm at 3 dB, intrinsically narrower than those of edge couplers, and polarization dependence remains their principal drawback.

Taken together, Tables 1 and 2 show that the two coupling families occupy complementary application spaces. Edge couplers offer lower loss (best 0.24 dB), broader bandwidth (up to 180 nm at 0.5 dB), and lower PDL, but require polished facets, edge access, and tighter positional alignment. Grating couplers provide placement flexibility, wafer-level testing, vertical packaging, and—crucially for cryogenic integration—a larger positional tolerance, which can accommodate part of the thermally induced displacement discussed in Section 4. This tolerance advantage, combined with fiber-array compatibility, makes grating interfaces preferable in current cryogenic TFLN packages, whereas edge/adiabatic interfaces are chosen when the adhesive is completely eliminated from the coupling region.

4 Research Progress on Fiber-to-Chip Cryogenic Packaging Technologies for Lithium Niobate Photonic Chips

When photonic chips operate in extremely low-temperature environments (a

few K to mK), the coupling system faces a core technical challenge arising from the mismatch of coefficients of thermal expansion [23]. The fiber-to-chip interface, precisely aligned and cured at room temperature, experiences significant relative displacement and stress when cooled to a few kelvin or even millikelvin, due to the differences in thermal expansion among the optical fiber (silica), chip substrate (lithium niobate/silicon), and packaging adhesive. This can lead to severe degradation of coupling efficiency or even complete device failure [51]. Two technical approaches can be adopted to address this issue.

From a mechanics standpoint, this mismatch can be formulated quantitatively. When the assembly is cooled by ΔT (e.g., 295 K from room temperature to liquid-helium temperature), each constituent undergoes an integrated free contraction

$$\varepsilon i = \frac{\Delta Li}{Li} = \int \alpha_i(T)\, dT \approx \bar{\alpha}_i \Delta T \tag{4}$$

where $\bar{\alpha}_i$ is the temperature-averaged coefficient of thermal expansion (CTE). Because the fiber, chip and cured adhesive are bonded together, this differential contraction must be accommodated either by elastic strain or by relative displacement at the coupling interface. For an idealized fully constrained joint, the cured adhesive develops a thermal (shear) stress

$$\sigma_{th} \approx Ea(\bar{\alpha}_a - \bar{\alpha}_s)\Delta T \tag{5}$$

where Ea is the adhesive modulus and the subscripts a and s denote adhesive and substrate (fiber/chip); if the bond lies a characteristic distance L_{eff} away from the coupling point, the corresponding lateral displacement of the fiber tip scales as

$$\delta_{th} \approx (\bar{\alpha}_a - \bar{\alpha}_s)\Delta T \cdot L_{eff} \tag{6}$$

Table 3 compiles representative thermomechanical parameters. The contrast is severe: the CTE of cured optical epoxies ((50–60) $\times 10^{-6}$ K^{-1} below the glass-transition temperature) is one to two orders of magnitude larger than that of fused silica (0.55×10^{-6} K^{-1}) and silicon (2.6×10^{-6} K^{-1}), while anisotropic lithium niobate lies in between (7.5×10^{-6} K^{-1} along c and 15.4×10^{-6} K^{-1} along a). Taking EPO-TEK 301-2 ($\alpha = 61\times10^{-6}$ K^{-1}, $E\approx3.0$ GPa) bonded to a silica fiber as an example, $(\alpha_a-\alpha_s)\Delta T \approx 60.5\times10^{-6}\times295 \approx 1.78\%$. A bond only $L_{eff} = 100$ μm from the interface

would therefore drive a displacement δ_{th}≈1.8 μm, already comparable to the ≈±1 μm 1-dB lateral tolerance of a grating coupler[25]; at L_{eff} = 1 mm the displacement reaches ≈18 μm, an order of magnitude beyond any coupler's capture range. Under full constraint, the same mismatch would generate σ_{th} ≈ 3.0 GPa×1.78% ≈ 53 MPa in the adhesive, comparable to or exceeding the typical lap-shear strength of optical epoxies (tens of MPa), which accounts for the adhesive cracking and occasional fiber detachment observed during cooldown. Moreover, once a polymer adhesive cools below its glass-transition temperature it becomes stiffer and more brittle, so the low-temperature Young's modulus—not the room-temperature value—governs the residual stress.

Table 3. Representative thermomechanical parameters of the constituent materials in TFLN cryogenic packages

Material	**Function in package**	**Mean CTE α (10^{-6} K^{-1})**	**T_g (°C)**	**Young's modulus at RT (GPa)**	**Estimated contraction, 300→4K (ΔL/L)**
Fused silica	Optical fiber	0.55	—	≈72	≈−1.1×10^{-4} (−0.011%)
Silicon	Carrier substrate	2.6	—	130–170	≈−2.2×10^{-4} (−0.022%)
Lithium niobate	Waveguide chip	15.4 (a-axis); 7.5 (c-axis)	—	120–170	≈ −(2–4)×10^{-3}
NTT-AT6001 (UV acrylate)	Rapid temporary pre-fix	not disclosed	≈0	compliant grade	order of 10^{-2}
EPO-TEK 301-2 (two-part epoxy)	Structural reinforcement	61 (below Tg)	≥80	≈3.0	≈ −(1–2)×10^{-2}
NOA86 (UV acrylate)	Remote strain relief	not disclosed	—	≈2.5	order of 10^{-2}

Note: Typical values compiled from manufacturer datasheets (NTT-AT, Epoxy Technology, Norland) and standard materials handbooks; the contractions are order-of-magnitude estimates obtained by integrating the mean CTE over 300–4 K. The modulus of polymer adhesives increases and the materials become more brittle upon cooling below T_g.

The first approach uses a cryogenic nanopositioning stage to track and correct the coupling position in real time during cooling. However, this method has inherent drawbacks: precision stages occupy valuable space in the cryogenic chamber, limit the number of input/output channels, introduce additional heat load, and are

susceptible to vibration noise in the vacuum cryogenic environment [52]. The second approach—cryogenic-compatible packaging technology—performs the alignment, fixing, and curing of the fiber and chip at room temperature, using material selection, stress management, and structural design to ensure that the packaged assembly maintains stable coupling performance after extreme temperature cycling. Clearly, the latter is the preferred path toward practical cryogenic deployment of photonic chips [26].

Equations (4)-(6) also rationalize the four packaging strategies reviewed below, each suppressing a different term of the mismatch. The two-step strategy pairs a fast UV acrylate for precise pre-alignment with a tough cryogenic-grade epoxy for load bearing, and selects the two adhesives for matched refractive indices (≈1.5) and matched thermal contraction, thereby minimizing the net δ_{th}; localized coating restricts the bonded area to the side surfaces to avoid stress concentration beneath the fiber; van der Waals assembly drives the adhesive CTE at the optical interface to zero by removing adhesive altogether (bonding only the fiber jacket ≈200 μm away), leaving a compliant free fiber span that absorbs differential strain; and photonic wire bonding replaces the rigid adhesive volume with a free-form polymer waveguide whose geometry is pre-compensated for polymerization and thermal shrinkage. These considerations turn adhesive selection from an empirical trial into a CTE–modulus–geometry co-design problem.

4.1 Two-Step UV–Epoxy Packaging

To meet the cryogenic packaging requirements of the TFLN platform, Wang et al. [54] proposed a temperature-insensitive packaging strategy. As shown in Fig. 11, a fast-curing UV adhesive (NTT-AT6001) is first used to pre-align and temporarily fix the fiber array to the chip, followed by reinforcement packaging with a two-component epoxy (EPO-TEK 301-2) that has higher toughness at low temperatures. This two-step method achieved a coupling efficiency of 15.7% ± 0.3%, with efficiency fluctuations of only ±0.5% over the temperature range of 1.5–295 K, and the performance remained stable after five thermal cycles, demonstrating excellent temperature insensitivity. The core innovation lies in the two-step curing

strategy: the UV adhesive provides rapid pre-fixing to ensure alignment accuracy, while the epoxy provides low-temperature toughness to ensure thermal cycling stability. This scheme effectively avoids the problems of brittle fracture or excessive thermal mismatch of a single adhesive at low temperatures, providing a practical solution for cryogenic packaging of TFLN photonic chips [25].

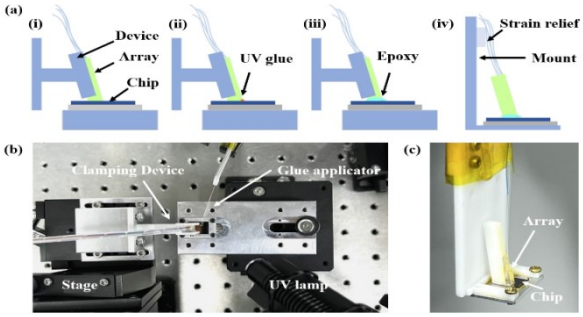


Fig. 11 Schematic of the two-step UV–epoxy packaging scheme. (a) Packaging process: (i) precise alignment of the fiber array to the target grating coupler; (ii) application of a small drop of UV adhesive on one side of the fiber array; (iii) complete coverage of the bottom of the fiber array with a large drop of two-component epoxy; (iv) transfer of the packaged chip to a mount ready for installation on the cryogenic sample rod. (b) Photograph of the packaging setup. A spare SMF-28 fiber fixed on a three-axis stage is used as the applicator. (c) Photograph of the packaged chip, which has been transferred to the mount ready for installation on the cryogenic sample rod.

4.2 Localized Adhesive Coating Packaging

Witt et al. [54] proposed a thermal-shock-resistant optical packaging method for thin-film lithium niobate devices, with the packaged device shown in Fig. 12. Through appropriate structural design and material selection, the packaged device is capable of cryogenic operation and can withstand extreme thermal shock.

The key to thermal-shock-resistant packaging lies in balancing thermal stress through structural design (e.g., applying adhesive only to the side surfaces rather than the bottom) and material selection (choosing epoxy with excellent low-temperature toughness), thereby avoiding structural failure due to stress concentration during temperature cycling. This scheme is particularly important for quantum optics experiments that require frequent room-temperature-to-cryogenic cycling, ensuring that the packaged device maintains stable optical coupling performance after multiple thermal cycles.

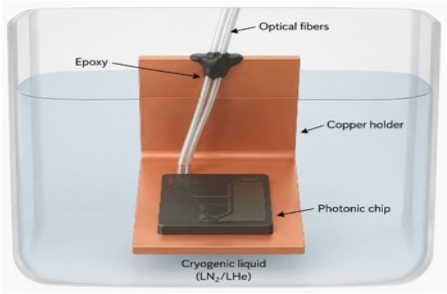


Fig. 12 Photograph of the localized adhesive coating packaging scheme.

4.3 van der Waals-Assisted Packaging

Zeng et al. [54] reported a packaging technique based on van der Waals assistance, as shown in Fig. 13. This technology achieves stable, low-loss fiber-to-chip coupling over the temperature range from room temperature down to 30 mK. The core innovation is that the contact between the fiber taper and the chip waveguide is maintained entirely by van der Waals forces rather than relying on adhesive. The adhesive is applied only to the fiber jacket about 200 μm away from the coupling interface for strain relief.

The key advantage of this design is that the adhesive is completely removed from the sensitive optical coupling region, so the optical properties of the adhesive are no longer a constraint, greatly expanding the choice of adhesives. At the same time, the purity of the coupling interface is preserved, avoiding the influence of adhesive refractive index on coupling efficiency. This technology has been successfully applied to TFLN ridge waveguides, achieving a coupling loss better than 3.5 dB/facet.

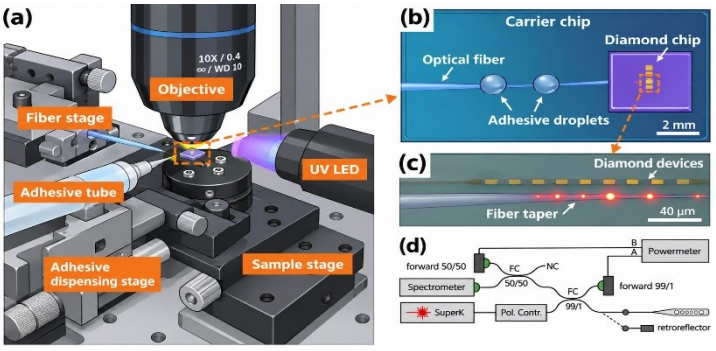


Fig. 13 van der Waals-assisted packaging scheme. (a) Customized alignment and assembly station for fiber manipulation and gluing; (b) Fiber-packaged device on a 20×15 mm² SiN-on-Si carrier chip under UV illumination, showing a series of adhesive droplets; (c) Optical image of the fiber-coupled diamond nanophotonic device; (d) Fiber network for coupling loss measurement.

4.4 Photonic Wire Bonding Packaging

Photonic wire bonding is an emerging optical interconnection technology that uses two-photon polymerization to 3D-print polymer optical waveguides. This technology directly writes three-dimensional free-form polymer waveguides between the fiber end face and the chip waveguide through two-photon polymerization, enabling efficient optical coupling within a ±30 μm alignment tolerance—the assembly process requires no active feedback alignment, only image recognition for positioning. Franken et al. [55] applied photonic wire bonding technology to the TFLN platform, as shown in Fig. 14. This scheme uses polymer waveguides fabricated by two-photon polymerization as the optical bridge between the fiber and the TFLN chip, achieving stable optical coupling at 5 K. The core advantage of this technology lies in its free-form waveguide design, which can adapt to optical ports of different mode-field sizes, and the low-temperature shrinkage of the polymer material can be compensated through flexible design of the waveguide structure.

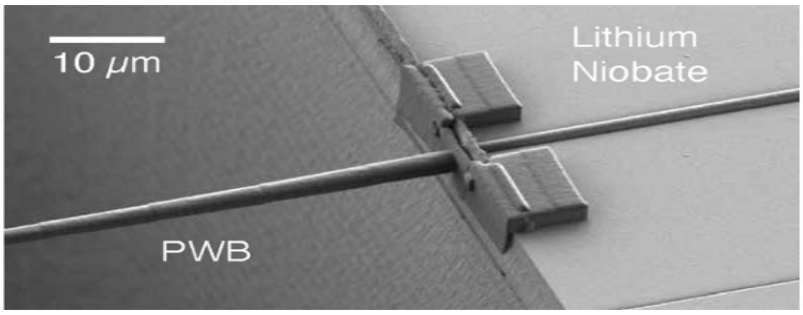


Fig. 14 Scanning electron microscope image of photonic wire bonds with anchoring structures connected to TFLN waveguides.

Table 4 summarizes the coupling methods, adhesives, operating temperatures, coupling efficiencies, and other key parameters of fiber-to-chip cryogenic packaging schemes for lithium niobate photonic chips reported in recent years.

Table 4. Summary of typical cryogenic packaging techniques for TFLN photonic chips

Package scheme	Coupling method	Fiber type	Adhesive/material	Temp.(K)	Coupling efficiency	Thermal cycling stability	Ref.
Two-step UV-epoxy packaging	Grating coupling	4-channel fiber array (SMF-28)	NTT-AT6001 + EPO-TEK 301-2	1.5–295	15.7% ± 0.3%	±0.5% fluctuation, stable over 5 cycles	[25]

Localized adhesive coating packaging	Grating coupling	Fiber array	Optimized epoxy	77-300	—	Resistant to extreme thermal shock	错误!未找到引用源。
van der Waals-assisted packaging	Adiabatic coupling	Tapered fiber	NOA 86TLH (away from coupling region)	0.03–300	44.67%	Stable	[54]
Photonic wire bonding packaging	Polymer waveguide	Fiber	Two-photon polymer	5	—	58 h operation without mode hopping	[55]

Note:All listed results are experimentally measured.

Table 3 compares the four cryogenic packaging strategies in terms of adhesive placement, minimum operating temperature, stability mechanism, and scalability. Two-step UV–epoxy packaging is the only scheme demonstrated with a multi-channel fiber array and exhibits an efficiency fluctuation of only ±0.5% over 1.5–295 K across five cycles; its stability arises from matched dual-adhesive contraction (Eqs. (5)–(6)) rather than from eliminating the adhesive. Localized coating achieves extreme thermal-shock resistance by restricting the adhesive to the sidewalls, at the expense of some automation. Van der Waals assembly achieves the lowest base temperature (30 mK) and the lowest loss (<3.5 dB/facet) by removing adhesive from the optical path, but relies on delicate tapered-fiber placement that is less compatible with parallel fiber-array integration. Photonic wire bonding provides the largest assembly tolerance (±30 μm without active alignment) and stable operation at 5 K, at the cost of a two-photon-lithography process. Overall, adhesive-free or remote-adhesive schemes offer advantages in ultimate operating temperature and interface loss, whereas adhesive-engineering schemes offer advantages in channel scalability and assembly throughput. These strategies should therefore be evaluated in conjunction with the CTE–modulus parameters in Table 3, rather than solely on the basis of coupling loss.

5 Conclusion and Outlook

This paper has systematically reviewed the recent progress in fiber-to-chip coupling and cryogenic packaging technologies for thin-film lithium niobate photonic chips. For edge coupling, a variety of schemes—including bi-layer inverse tapers, tri-layer inverse tapers, three-dimensional inverse tapers, trident structures, wedge-shaped couplers, double-layer metasurfaces, and multilayer silicon nitride-assisted structures—have achieved coupling losses below 0.5 dB/facet, with bandwidths covering the C+L bands and even extending into the visible range, along with significantly improved fabrication tolerances. For grating coupling, chirped gratings, apodized gratings, suspended gratings, hybrid silicon-platform gratings, and vertical gratings with bottom metal mirrors have made continuous progress, achieving sub-dB coupling losses and broadband operation. For cryogenic packaging, innovative approaches such as two-step UV–epoxy packaging, localized adhesive coating packaging, van der Waals-assisted packaging, and photonic wire bonding packaging have preliminarily addressed the coupling stability challenges from room temperature down to millikelvin temperatures. Taken together, Tables 1–4 show that sub-dB edge coupling is best achieved with multi-layer adiabatic tapers, whereas cryogenic packaging typically relies on high-tolerance grating interfaces. In addition, simulation-only designs tend to overestimate coupling performance by approximately 0.3–0.9 dB compared with measured devices.

Nevertheless, the current technologies are not yet fully mature. Key issues including the scalable fabrication of edge couplers, the trade-off between efficiency and bandwidth for grating couplers, and the long-term reliability of cryogenic adhesives in the mK regime remain the main bottlenecks restricting the widespread deployment of TFLN photonic chips. Looking forward, systematic characterization of the mechanical and optical properties of adhesives at cryogenic temperatures will provide guidance for material selection. Novel packaging materials combining low loss, excellent low-temperature toughness, and convenient curing properties are expected to overcome existing technical barriers. Advances in tapered fiber arrays and multi-channel parallel fabrication techniques will pave the way for high-density optical interconnects in cryogenic applications. With the continued evolution of these

key technologies, cryogenic-compatible lithium niobate photonic packaging will provide essential foundational support for frontier quantum information systems, including superconducting quantum computing, quantum networks, and single-photon detection.

This work was supported by the National Key R&D Program of China (Grant No. 2025YFA1212603)

References

[1] Desiatov B, Shams-Ansari A, Zhang M, Wang C and Lončar M 2019 Optica 6 380
[2] Luo Q, Bo F, Kong Y and Zhang G 2021 Chin. Opt. Lett. 19 060003
[3] Wang M, Chen Q, Li H, Zhang J and Liu Y 2023 Adv. Quantum Technol. 6 2300005
[4] Li M, Liang H, Luo R, He L and Lin Q 2019 Opt. Express 27 35560
[5] Wang C, Zhang M, Chen X, Bertrand M, Shams-Ansari A, Chandrasekhar S, Winzer P and Lončar M 2018 Nature 562 101
[6] Zhang M, Buscaino B, Wang C, Shams-Ansari A, Reimer C, Zhu D and Lončar M 2019 Nature 568 373
[7] Wang C, Langrock C, Marandi A, Zhao M, Zhang M, Fejer M M and Lončar M 2018 Optica 5 1438
[8] Zhu D, Shao L, Yu M, Cheng R, Desiatov B, Xin C J, Hu Y, Holzgrafe J, Ghosh S, Shams-Ansari A, Puma E, Sinclair N, Reimer C, Zhang M and Lončar M 2021 Adv. Opt. Photonics 13 242
[9] Xue Y, Gan Y, Zhang Y, Liu H and Li Z 2022 Nanophotonics 11 1121
[10] Chen G, Li H, Chen K and Xu Y 2024 APL Photonics 9 011301
[11] Boes A, Corcoran B, Chang L, Bowers J and Mitchell A 2018 Laser Photon. Rev. 12 1700256
[12] Lin J, Bo F, Cheng Y and Xu J 2020 Photonics Res. 8 1910
[13] Zhang M, Wang C, Kharel A, Zhu D and Lončar M 2022 Nat. Photonics 16 395
[14] Krasnokutska I, Tambasco J L J and Peruzzo A 2019 Opt. Express 27 16578
[15] Sun D W, Zhang Y, Wang D and Li M 2023 Acta Phys. Sin. 72 124201 (in Chinese)
[16] Son G, Han S, Park J, Kwon K and Yu K 2018 Nanophotonics 7 1845
[17] Marchetti R, Lacava C, Carroll L and Reed G T 2019 Photonics Res. 7 201
[18] Li H, Zhou H, Zhang J and Chen X 2020 J. Phys. Photonics 2 044004
[19] Zhou J, Gao R, Lin J and Wang M 2021 Opt. Lett. 46 525
[20] Riedinger R, Wallucks A, Marinković I, Löschnauer C, Aspelmeyer M, Hong S and Gröblacher S 2018 Nature 556 473

[21] Sprengers J P, Gaggero A, Sahin D, Jahanmirinejad S, Frucci G, Mattioli F, Leoni R, Beetz J, Lermer M, Kamp M, Höfling S, Sanjines R and Fiore A 2011 Appl. Phys. Lett. 99 181110
[22] McKenna T P, Witmer J D, Patel R N and Safavi-Naeini A H 2020 Optica 7 1737
[23] Youssefi A, Shomroni I, Joshi Y J and Kippenberg T J 2021 Nat. Electron. 4 326
[24] Witt D, Chrostowski L and Young J 2025 Appl. Phys. Lett. 127 021105
[25] Wang Y T, Ma Y X, Wang X J, Zhao Z W, Li Y M and Yang T S 2025 Photonics 12 545
[26] Zhao Z W and Yang T S 2026 Laser Optoelectron. Prog. 63 2100006 (in Chinese)
[27] Chen B, Ruan Z, Hu J and Chen K 2021 Opt. Express 29 1289
[28] Ma Y X, Wang Y T and Yang T S 2025 Laser Optoelectron. Prog. 62 1127008 (in Chinese)
[29] Ma X, Zhuang C, Zeng R and Zhang Y 2020 Opt. Express 28 17113
[30] Chen B, Ruan Z, Chen K and Fan X 2023 Opt. Lett. 48 1434
[31] Zheng Y R, Yuan J M, Mao Y Z and Wang A 2026 Acta Photonica Sin. 55 0213001 (in Chinese)
[32] He L Y, Zhang M, Shams-Ansari A, Zhu R R, Wang C and Lončar M 2019 Opt. Lett. 44 2314
[33] Hu C R, Pan A, Li T A, Wang X H, Liu Y H, Tao S Q, Zeng C and Xia J S 2021 Opt. Express 29 5397
[34] Ying P, Tan H, Zhang J and Cai X 2021 Opt. Lett. 46 1478
[35] Liu X, Gao S, Zhang C, Wang Y and Li Z 2022 Adv. Photon. Nexus 1 016001
[36] Chen B, Ruan Z, Wang M and Fan X 2024 APL Photonics 9 116111
[37] Li Z, Hao T, Zhou D and Chen S 2025 IEEE Photonics J. 17 2201306
[38] Ma R, Yuan C, Sun J and Zhang H 2025 Opt. Lett. 50 7203
[39] Zou X, Li H L, Choi D Y, Kim J T and Lee S S 2026 Sci. Rep. 16 2493
[40] Tang Y, Chen Q, Dai X and Wang L 2025 Opt. Lett. 50 5558
[41] Jian J, Xu P, Chen H and Li Z 2018 Opt. Express 26 29651
[42] Kang S T, Zhang R, Hao Z Z, Jia D, Gao F, Bo F, Zhang G Q and Xu J J 2020 Opt. Lett. 45 6651
[43] Kang S T, Gao F, Yu X Y, Bo F, Zhang G Q and Xu J J 2023 J. Opt. Soc. Am. B 40 D21
[44] Wang H R, Du Y C, Lin T, Lu J P and Ni Z H 2025 Opt. Commun. 593 132277
[45] Suraj, Bhageri M and Yi L 2026 Appl. Phys. Lett. 128 204005
[46] Yuan H, Mao X and Yuan Z 2024 Opt. Continuum 3 2369
[47] Lu J D, Chen G Y, Su W Q, Li H B, Gu X W and Yu H 2025 Opt. Express 33 28226
[48] Cai L and Piazza G 2019 J. Opt. 21 065801
[49] Fang S B, Hong B Z, Lv L M, Shen R Y, Zhao H B, Chu W, Cai H W and Huang W P 2024 Opt. Lett. 49 5519
[50] Wang H H, Qi L, Chen B, Gan R F, Ruan Z L, Cui A, Guo C J, Chen K X and Liu L 2025 Chin. Opt. Lett. 23 051301
[51] Wasserman W W, Harrison R A, Harris G I, Sawadsky A, Sfendla Y L, Bowen W P and Baker C G 2022 Opt. Express 30 30822

[52] McKenna T P, Patel R N, Witmer J D, Van Laer R, Valery J A and Safavi-Naeini A H 2019 Opt. Express 27 28782
[53] Witt D, Warner H K, Rajabali S and Lončar M 2024 CLEO, JTh2A.115
[54] Zeng B, De-Eknamkul C, Assumpcao D, Renaud D, Wang Z X, Riedel D, Ha J, Robens C, Levonian D, Lukin M, Riedinger R, Bhaskar M, Sukachev D, Lončar M and Machielse B 2023 Appl. Phys. Lett. 123 161106
[55] Franken C A A, Cheng R, Powell K, Kyriazidis G, Rosborough V, Musolf J, Shah M, Barton III D R, Hills G, Johansson L, Boller K J and Lončar M 2025 APL Photonics 10 026107